Classification: Physical Sciences: Chemistry; Biological Sciences: Medical Sciences

Mucinase-engineered cell membrane nanovesicles degrade the glycocalyx shield to potentiate antitumor immunity

Running title: Breaking the glycocalyx shield with nanoengineered mucinase for cancer immunotherapy

Xiaorui Geng[a,1], Silan Liu[a,b,1], Yuanwei Pan[a], Yun Ge[a,c,2], and Lang Rao[a,2]

[a] Institute of Chemical Biology, Shenzhen Bay Laboratory, Shenzhen 518132, China.

[b] Shenzhen Medical Academy of Research and Translation (SMART), Shenzhen 518107, China.

[c] State Key Laboratory of Chemical Oncogenomics, School of Chemical Biology and Biotechnology, Peking University Shenzhen Graduate School, Shenzhen 518055, China.

[1] X.G. and S.L. contributed equally to this work.

[2] Corresponding e-mail: geyun@szbl.ac.cn (Y.G.); lrao@szbl.ac.cn (L.R.).

Abstract

The tumor glycocalyx forms a protective shield that masks checkpoint proteins and compromises the efficacy of immunotherapies. While the bacterial protease StcE can degrade this barrier by cleaving O-glycosylated mucin domains, its therapeutic potential is hindered by off-target toxicity and high immunogenicity. To overcome these limitations, we developed a biomimetic platform of cell membrane fusion nanovesicles (FNVs) that co-display StcE and CD47 nanobodies (nCD47) for spatially controlled glycocalyx degradation and enhanced checkpoint blockade. Using the SpyTag/SpyCatcher system, we first generated StcE-displaying NVs, which were then fused with nCD47-displaying NVs. The resulting StcE-nCD47-FNVs retained potent mucin-hydrolyzing activity and exhibited well-defined physicochemical properties. By removing the mucin barrier, StcE-nCD47-FNVs significantly enhanced nCD47 binding to CD47 on tumor cells, thereby potentiating antitumor immune responses. More importantly, benefiting from the prolonged circulation of FNVs and the tumor-targeting capability of nCD47, the StcE-nCD47-FNVs platform demonstrated superior tumor accumulation and biosafety compared to free StcE. In murine models of colorectal and breast cancer, StcE-nCD47-FNVs significantly suppressed tumor growth and metastasis by remodeling the tumor microenvironment, as evidenced by increased M1 macrophage polarization and $CD8^+$ T cell infiltration. By integrating glycocalyx engineering with vesicle nanotechnology, StcE-nCD47-FNVs offer a safe, robust, and versatile strategy to breach the tumor glycocalyx for next-generation cancer immunotherapy.

Keywords: Glycoengineering, Nanobiotechnology, Cellular vesicles, Drug delivery, Cancer immunotherapy.

Significance Statement

The tumor glycocalyx limits antibody access to surface receptors, underscoring the need for strategies that degrade this barrier to enhance checkpoint blockade therapy. This study pioneers a tumor-targeted glycocalyx-degrading platform that synergizes mucinase activity with checkpoint blockade to overcome therapeutic resistance. By engineering fusion nanovesicles co-displaying bacterial protease StcE and CD47 nanobodies, the resulting StcE-nCD47-FNVs platform achieves localized glycocalyx removal while enhancing CD47-SIRPα axis blockade, thus boosting macrophage phagocytosis and cytotoxic T cell infiltration. Benefiting from superior tumor accumulation and biosafety, this strategy significantly suppresses tumor growth and metastasis in colorectal and breast cancer models. By combining glycocalyx engineering with checkpoint blockade, this work offers a blueprint for next-generation immunotherapies against physical and molecular barriers in solid and metastatic tumors.

Introduction

Immune checkpoint blockade (ICB) therapy activates antitumor immune responses by using antibodies to block immune checkpoints (1, 2). Among these, the CD47-SIRPα axis has attracted interest for its role in suppressing macrophage phagocytosis (3). Although monoclonal antibodies targeting CD47-SIRPα, such as Magrolimab and Lemzoparlimab (4), have shown encouraging preclinical results, they still exhibit limited effectiveness in clinical trials (5). The glycocalyx on the surface of tumor cells act as a potential obstacle for ICB therapy (6). In tumors such as breast and colorectal cancers, aberrant overexpression and glycosylation of mucins (*e.g.*, MUC1, MUC2, and MUC5AC) result in the formation of a glycocalyx layer hundreds of nanometers thick (7, 8). This dimensions far exceeds the heights of therapeutic targets such as HER2 (~15 nm) (9), PD-L1 (~7 nm) (10) and CD47 (~10 nm) (11), thereby impeding the binding of drugs. Therefore, developing strategies to effectively degrade the mucin-rich glycocalyx and expose masked immune checkpoint targets is critical for enhanced ICB therapy.

Current strategies targeting the glycocalyx mainly focus on inhibiting mucin synthesis or glycosylation (12). However, these approaches cannot effectively remove the pre-existing glycocalyx. In contrast, direct enzymatic degradation represents a more efficient solution (13). Among the potential

enzymatic candidates, the secreted protease of C1-esterase inhibitor (StcE) from *Escherichia coli* can precisely cleave heavily O-glycosylated mucin domains, thereby efficiently removing the glycocalyx from cell surfaces (14). Despite its potential, the broad application of StcE is limited by considerable safety concerns. On one hand, glycocalyx is widely expressed in normal tissues, systemic administration of StcE may cause non-specific tissue damage (15). On the other hand, as a bacterial-derived recombinant protease, StcE possesses inherent immunogenicity that may trigger adverse inflammatory responses *in vivo* (16). Therefore, improving the biocompatibility and tumor selectivity of StcE is critical for its effective integration into ICB therapy.

Given that the majority of proteins are membrane proteins (17), cellular nanovesicles (NVs), generated through scalable reconstitution and self-assembly of natural cell membranes, represent an attractive platform for co-delivery of StcE and nCD47 (18). Endowed with inherent tumor-targeting capability, low immunogenicity, and prolonged circulation, NVs are expected to decrease off-selective toxicity and improve the biocompatibility of StcE (19). Moreover, the engineerability of NVs offers distinct advantages over traditional antibody-enzyme conjugation methods, which often suffer from loss of enzymatic activity due to random chemical coupling or inefficient expression of large fusion proteins (20, 21). In particular, NVs enable the co-display of StcE and nCD47 through precise engineering. Our previous work demonstrated the successful surface display of nCD47 on NVs (22), whereas direct genetic fusion of large

proteins such as StcE remains challenging. To overcome this limitation, the SpyTag-SpyCatcher system can be employed to achieve controllable, topology-specific covalent conjugation while preserving enzymatic activity (23, 24). Therefore, NVs provide an efficient platform to safely and controllably degrade the glycocalyx, enabling synergistic integration with immune checkpoint blockade therapy.

Herein, we report the development of engineered fusion NVs as a versatile platform co-displaying StcE and nCD47 *via* the SpyTag-SpyCatcher system. The resulting StcE-nCD47-FNVs effectively degraded the glycocalyx, exposing the masked CD47 epitopes on tumor cells and enhancing the blockade of the CD47-SIRPα axis. Moreover, the co-displayed of nCD47 imparted StcE-nCD47-FNVs to anchor to the tumor surface post-degradation of mucin, establishing a positive feedback loop that concentrates the hydrolytic activity of StcE at the tumor site to mitigate non-specific toxicity. In both colorectal cancer and breast cancer lung metastasis models, treatment with StcE-nCD47-FNVs remodeled the tumor microenvironment by enhancing the infiltration of M1 macrophages and $CD8^+$ T cells. This synergistic integration of targeted glycocalyx degradation with ICB, translated into enhanced efficacy in suppressing tumor growth and metastasis.

Results

Display of StcE on cell surfaces *via* a bioconjugation strategy

The dense glycocalyx on the tumor cell surface presents a physical barrier that sterically hinders the binding of therapeutic agents, such as nCD47, to immune checkpoints like CD47 (25). To overcome this, we developed nanovesicles (NVs)-based system utilizing the mucin-specific protease StcE, hypothesizing that targeted degradation of the glycocalyx would unmask these underlying epitopes (Fig. 1*A*). Firstly, StcE and its inactive mutant (StcE E447D, hereafter denoted as

StcE*), were expressed and purified as previously reported (Fig. S1*A*) (26). The enzymatic activity of StcE was verified by cleavage of the recombinant C1 esterase inhibitor (C1INH) substrate (Fig. S1*B*) and reduction of MUC1 levels on HeLa cells (Figures S2). Moreover, AF647-labeled StcE* was validated as an effective mucin probe, exhibiting a staining pattern comparable to commercial anti-MUC1 antibodies (Fig. S2*B*). Staining with AF647-StcE* revealed that various mouse tumor cell lines, including 4T1, CT26, and B16F10, expressed surface mucins that were highly susceptible to StcE-mediated degradation (Fig. 1*B-C*). These findings demonstrated that StcE could effectively remove the mucin on various cancer cells.

Given that NVs function as biocompatible carriers for surface enzyme presentation (27), we first aimed to display StcE on HEK293T cells. Direct membrane display of HA-tagged StcE or StcE* on HEK293T cells via lentiviral transduction failed to yield detectable expression, likely due to the high molecular weight and potential toxicity of StcE (Fig. S3). Therefore, an indirect bioconjugation strategy was adopted using the SpyTag003 (ST)-SpyCatcher003 (SC) system, which spontaneously forms a covalent isopeptide bond (28). HEK293T cells were engineered to express SC (HEK293T-SC) for covalent conjugation of StcE bearing ST (StcE-ST) (Fig. 1*D*). Cleavage assays confirmed that StcE-ST retained enzymatic activity comparable to StcE against both C1INH and mucins on HeLa cells (Fig. S1*B*, S4). SDS-PAGE demonstrated efficient *in vitro* conjugation of StcE-ST and SC (Fig. S5). Robust surface HA-tagged SC expression on HEK293T was confirmed by flow cytometry (Fig. S6). Subsequent incubation of HEK293T-SC cells with StcE-ST resulted in successful and covalent surface conjugation, as verified by both western blotting and flow cytometry (Fig. 1*E-F*). Ligation was achieved with 0.1 μM StcE-ST, whereas higher concentrations (>2 μM) caused non-specific binding (Fig. 1*G-I*). These results

validate the establishment of a controllable platform using engineered HEK293T-SC cells for the robust surface display of high-molecular-weight enzymes.

Preparation and characterization of fusion cellular vesicles

Having established a platform for StcE display, we next evaluated the ability of the engineered HEK293T-StcE cells to remove mucins from tumor cell surfaces (Fig. 2*A*). Flow cytometry confirmed that HEK293T-StcE cells, effectively degraded MUC1 on HeLa cells (Fig. 2*B*). This system enabled controlled mucin degradation on HeLa cells through titration of StcE-ST concentrations (Fig. 2*C*). Moreover, HEK293T-StcE cells also efficiently degraded mucins on the surface of both CT26 and 4T1 cells, indicating broad applicability (Fig. 2*D*-*G*). We then prepared nanovesicles (StcE-NVs) from these engineered cells via sonication and extrusion. The resulting StcE-NVs retained potent mucinase activity, successfully reducing MUC1 levels on HeLa cells, whereas control vesicles derived from StcE*-expressing cells (StcE*-NVs) showed no effect (Fig. S7). StcE-NVs maintained stable hydrolysis activity for at least one week when stored at 4°C (Fig. S8). However, StcE-NVs lacked tumor-targeting ability because they were derived from normal cells without inherent homing capacity, and StcE itself does not exhibit cell-type specificity.

To enhance the tumor targeting and therapeutic potential, StcE-NVs were fused with nCD47-NVs derived from 4T1/CT26-nCD47 cells to generate StcE-nCD47-FNVs, while StcE*-NVs were fused in parallel to obtain StcE*-nCD47-FNVs (Fig. 2*H*). StcE-nCD47-FNVs significantly depleted MUC1 from the surface of HeLa cells across adjustable fusion ratios (Fig. 2*I*). A 1:3 mass ratio (StcE-NVs to nCD47-NVs) was selected for subsequent studies, as it provided optimal mucinase activity and high nCD47 expression. Western blotting confirmed the presence of both nCD47 and StcE-ST in StcE-nCD47-FNVs, consistent with inheritance from the parental vesicles (Fig. 2*J*). Confocal microscopy further verified successful membrane fusion, showing co-localization of DiI-labeled nCD47-NVs (red) and DiO-labeled StcE-NVs (green) (Fig. 2*K*, S9*A*). Physical

characterization revealed that StcE-nCD47-FNVs maintained a diameter of approximately 160 nm, a zeta potential of -25 mV, and a cup-shaped morphology, similar to the precursor vesicles (Fig. 2*L-M*, S9*B-D*). Crucially, the enzymatic function was preserved post-fusion. Flow cytometry showed that the mucinase activity of StcE-nCD47-FNVs against 4T1 cell-surface mucins was comparable to that of StcE-NVs (Fig. 2*M*). This work developed mucin degradation StcE-NVs capable of fusing with other functional vesicles, such as nCD47-NVs, to create StcE-nCD47-FNVs with enhanced tumor-targeting capability and improved therapeutic payload delivery.

StcE-nCD47-FNVs enhance tumor accumulation and improve systemic biocompatibility

High CD47 expression on tumor cells suppresses macrophage phagocytosis by engaging the SIRPα inhibitory receptor (29). StcE-nCD47-FNVs were designed to overcome this by simultaneously degrading the glycocalyx and blocking the CD47-SIRPα axis. First, we validated the binding specificity of the nCD47 component. Immunofluorescence imaging confirmed that FITC-labeled nCD47-NVs bound effectively to wild-type tumor cells but showed markedly reduced binding to CD47-knockdown (CD47KD) cells, confirming binding specificity (Fig. 3*A-C*, S10*A-C*). Notably, StcE-nCD47-FNVs exhibited even stronger binding to tumor cells than nCD47-NVs alone. This enhanced interaction is likely due to StcE-mediated degradation of the the glycocalyx, which exposes CD47 epitopes and thereby facilitates more efficient nCD47 binding (Figures 3*D-E*, S10*D*). Next, we investigated whether this enhanced binding translates to improved phagocytosis. Tumor cells pretreated with different NVs were co-incubated with M1 macrophages. Pretreatment with StcE-nCD47-FNVs resulted in a significant increase in macrophage-mediated phagocytosis compared to treatment with nCD47-NVs alone. This demonstrates that degrading the glycocalyx and blocking CD47 synergistically enhances the immune clearance of tumor cells

(Fig. 3*F-G*, S11).

In vivo studies in CT26 tumor-bearing mice showed that Cy5.5-labeled nCD47-NVs and StcE-nCD47-FNVs exhibited sustained tumor accumulation, whereas free StcE was rapidly cleared from circulation. These results were also confirmed by *ex vivo* imaging of dissected tumor tissues (Fig. 3*H*, S12). Crucially, displaying StcE on StcE-nCD47-FNVs significantly mitigated its systemic toxicity. Mice treated with free StcE developed severe adverse effects, including hematological abnormalities (*e.g.*, decreased platelets), periocular inflammation, and hepatotoxicity, as indicated by elevated liver enzymes (ALT, AST, LDH) (Fig. 3*I-K*, S13, S14). In contrast, the StcE-nCD47-FNVs treatment group exhibited normal hematological and biochemical profiles, with no histopathological changes observed in major organs. These in vivo safety findings were consistent with in vitro assays, which showed that the FNVs possessed excellent hemocompatibility and minimal cytotoxicity, whereas free StcE was both hemolytic and toxic to bEnd.3 cells (Fig. S15). Together, these findings indicate that StcE displayed on StcE-nCD47-FNVs enhances CD47 binding and promotes macrophage phagocytosis. The tumor-specific accumulation of StcE-nCD47-FNVs *in vivo* is critical for reducing StcE-associated toxicity.

In vivo antitumor efficacy of StcE-nCD47-FNVs in a subcutaneous tumor model

Encouraged by *in vitro* findings, we next evaluated the therapeutic efficacy of StcE-nCD47-FNVs in CT26 tumor-bearing mice. On day 7 post-inoculation, mice were randomized into five treatment groups and dosed intravenously every other day: G1 (PBS), G2 (FNVs), G3 (StcE-FNVs, glycocalyx hydrolysis only), G4 (nCD47-FNVs, CD47 blockade only), and G5 (StcE-nCD47-FNVs, combination) (Fig. 4*A*). While control groups (G1, G2) exhibited rapid tumor growth, all treatment groups showed different level of inhibition. The single-modality treatments (G3 and G4) only moderately suppressed tumor progression. In

contrast, the combination therapy in G5 produced a markedly potent anti-tumor effect, achieving a tumor inhibition rate of 95.83 ± 2.71%, (Figures 4*B-C*, S16). This enhanced efficacy is attributed to a synergistic mechanism where initial nCD47 binding facilitates StcE-mediated hydrolysis of the glycocalyx, which in turn exposed new epitopes to improve overall vesicle binding. Importantly, this potent efficacy was achieved without inducing significant body weight loss, indicating a favorable safety profile for the treatment (Fig. 4*D*). Survival analysis further confirmed these results, as the G5 mice showed significantly prolonged survival compared to all other groups (Fig. 4*E*).

To elucidate the immunological mechanisms underlying the observed therapeutic efficacy, we performed a detailed analysis of the tumor microenvironment. Flow cytometry revealed a comprehensive remodeling of the immune landscape in G5 tumors. This included a polarization of macrophages toward a pro-inflammatory M1-like phenotype, an increased infiltration of cytotoxic $CD8^+$ T cells and NK cells, and a reduction in immunosuppressive regulatory T cells (Fig. 4*F-I*, S19-S21). Consistent with this pro-inflammatory shift, cytokine analysis showed an upregulation of IFN-γ and IL-6 alongside a downregulation of TGF-β and IL-10 (Fig. S22). Transcriptomic analysis provided deeper insight into these changes. Principal component analysis (PCA) showed a clear distinction between the G5 and control groups, with 852 differentially expressed genes identified (Fig. S23*A-B*). Pathway analysis revealed that G5 treatment upregulated immune activation genes (Ifng, Ccl3) while downregulating genes associated with immunosuppression (Mmp23), proliferation (Egfr), and extracellular matrix (ECM) remodeling (Postn, Col6a3) (Fig. 4*J*). Furthermore, Gene Set enrichment analysis (GSEA) showed a negative enrichment negative enrichment for key oncogenic pathways, including PI3K-Akt, Wnt, and focal adhesion signaling (Fig. 4*K-L*, S23*C-E*). Collectively, these immune cellular and transcriptomic analyses confirm that StcE-nCD47-FNVs reverse immunosuppression and activate potent anti-tumor immune responses,

highlighting the synergistic interplay between StcE, nCD47, and NVs.

In vivo antitumor efficacy of StcE-nCD47-FNVs in a subcutaneous tumor model

To evaluate the efficacy of StcE-nCD47-FNVs in in a more stringent metastatic setting, we employed a 4T1 lung metastasis model. Mice were intravenously injected with luciferase-expressing 4T1 cells and subsequently randomized into five treatment groups: G1 (PBS), G2 (FNVs), G3 (StcE-FNVs), G4 (nCD47-FNVs), and G5 (StcE-nCD47-FNVs). Treatments were administered every two days, and tumor progression was monitored via *in vivo* bioluminescence imaging (Fig. 5*A*). After 21 days, both *in vivo* and *ex vivo* imaging revealed that the G5 (StcE-nCD47-FNVs) treatment exerted the most significant inhibitory effect on lung metastases (Fig. 5*B*). While the monotherapies (G3 and G4) provided a slight, limited therapeutic benefit, lungs from G5 group showed reduction in both the size and number of metastatic nodules, corresponding to a tumor inhibition rate of 92.90 ± 3.71% (Fig. 5*C-E*, S24*A*). Histological analysis via H&E staining further confirmed these findings. Crucially, the survival rate for mice treated with StcE-nCD47-FNVs was 100% at day 35, underscoring the potent therapeutic efficacy of the combination therapy in a metastatic setting (Fig. 5*F*).

We next investigated whether the anti-metastatic efficacy of StcE-nCD47-FNVs was driven by a similar activation of the immune system. Immunofluorescence staining of lung tissue from the G5 treatment group confirmed a significant remodeling of the immune microenvironment. Macrophages repolarized toward a pro-inflammatory M1 phenotype, evidenced by an increase in $CD86^+$ cells and a decrease in $CD206^+$ M2 cells (Fig. 5*G*). Furthermore, treatment with StcE-nCD47-FNVs significantly enhanced the infiltration of $CD8^+$ T cells into the lung tissue (Fig. S24*B*). This cellular reprogramming was accompanied by a robust change in the cytokine profile. The lungs of treated mice showed a significant upregulation of pro-inflammatory cytokines, including IFN-γ, TNF-α, and IL-1β, and a concurrent downregulation of

the immunosuppressive cytokine IL-10 (Fig. 5*H-K*). Collectively, these results demonstrate that StcE-nCD47-FNVs effectively reverses the immunosuppressive microenvironment in lung metastases. This potent immune activation, characterized by M1 macrophage polarization and cytotoxic T cell infiltration, underlies the therapy's ability to eliminate metastatic tumors and prolong survival.

Discussion

In this study, we developed a multifunctional fused cell-derived vesicle platform, StcE-nCD47-FNVs, that synergistically overcame tumor immune evasion by combining glycocalyx degradation with CD47 checkpoint blockade. StcE-NVs were first generated using the SpyTag–SpyCatcher system to efficiently hydrolyze mucins, and subsequently fused with nCD47-NVs, derived from engineered tumor cells, to form StcE-nCD47-FNVs with well-defined physicochemical properties while retaining mucin hydrolysis activity. By degrading the mucin barrier, StcE-nCD47-FNVs enhanced the binding of nCD47 to tumor-cell CD47, which blocked the CD47-SIRPα axis and significantly promoted macrophage phagocytosis. Furthermore, StcE-nCD47-FNVs possessed superior tumor accumulation and safety compared to free StcE *in vivo*. In two murine tumor models, StcE-nCD47-FNVs markedly inhibited primary tumor growth and metastasis, prolonged survival, and remodeled the tumor microenvironment by promoting M1 macrophage polarization and cytotoxic $CD8^+$ T cell infiltration.

The tumor glycocalyx is an emerging target for immunotherapy due to its critical role in immune evasion (30, 31). Although strategies like enzymatic glycan removal have shown promise (32), the interplay between glycocalyx degradation and ICB therapy remains underexplored. This work directly

addresses this gap, demonstrating that targeted glycocalyx degradation significantly enhances immune checkpoint blockade efficacy. Transcriptomic analysis revealed that this synergy is driven by a comprehensive remodeling of the tumor microenvironment, including the downregulation of key progression pathways (*e.g.*, PI3K-Akt and Wnt) and increased anti-tumor immune cell infiltration. Along with the increasing knowledge of the tumor glycocalyx grows, future efforts will focus on how its hydrolysis remodels the tumor microenvironment and on combining this strategy with targeting other surface proteins (33, 34). Such approaches could enhance the bioavailability and efficacy of a wide range of therapeutic agents.

Cell membrane nanovesicles (NVs) are ideal nanoplatforms for displaying large or non-specific proteins, as they are readily amenable to engineering (35). In this study, we employed the SpyTag/SpyCatcher technology to achieve a controllable, site-specific covalent conjugation of StcE, which successfully preserved its enzymatic activity. This versatile strategy could be extended to other nanoplatforms, allowing for the rapid functional modification of vesicles with a wide range of proteins, including therapeutic antibodies and cytokines that possess off-target toxicity or high molecular weight (36, 37). In conclusion, by synergistically combining glycocalyx degradation with immune checkpoint blockade, this work validates the potent anti-tumor efficacy of StcE-nCD47-FNVs. This work provides a solid foundation for the continued development of multifunctional nanotherapeutics, establishing a universal and modular framework that integrates glycocalyx degradation with other therapeutic agents for cancer immunotherapy in the future.

Methods

A detailed version of the experimental methods used in this article has been provided in the *SI Appendix*.

Data, materials, and software availability

All study data are included in the article and/or *SI Appendix*.

Acknowledgements

This work was supported by the Shenzhen Medical Research Found (No. B2502017), the National Natural Science Foundation of China (Nos. 82222035, 22277080, 92478103, and 82502547), the National Key R&D Program of China (No. 2024YFC3407200), and the Major Program of Shenzhen Bay Laboratory (No. S241101001).

Author Contributions

L.R. and Y.G. conceived the study. X.G. and S.L. designed the experiments. X.G. and S.L. performed the experiments. X.G. and S.L. analyzed the data. X.G., S.L., and Y.W. wrote the manuscript. All authors have given approval to the final version of the manuscript.

Competing Interests

The authors have filed a patent on this work and declare no other conflict of interest in this work. The submission is presently under review.

References

1. K. Aliazis et al., The tumor microenvironment's role in the response to immune checkpoint blockade. Nat. Cancer 6, 924-937 (2025).

2. M. Y. Feng et al., Phagocytosis checkpoints as new targets for cancer immunotherapy.

Nat. Rev. Cancer 19, 568-586 (2019).

3. M. E. W. Logtenberg, F. A. Scheeren, T. N. Schumacher, The CD47-SIRPα immune checkpoint. Immunity 52, 742-752 (2020).

4. R. Upton et al., Combining CD47 blockade with trastuzumab eliminates HER2-positive breast cancer cells and overcomes trastuzumab tolerance. Proc. Natl. Acad. Sci. USA 118, e2026849118 (2021).

5. R. Advani et al., CD47 blockade by Hu5F9-G4 and rituximab in non-hodgkin's lymphoma. N. Engl. J. Med. 379, 1711-1721 (2018).

6. C. R. Shurer et al., Physical principles of membrane shape regulation by the glycocalyx. Cell 177, 1757-1770 (2019).

7. J. C. H. Kuo, J. G. Gandhi, R. N. Zia, M. J. Paszek, Physical biology of the cancer cell glycocalyx. Nat. Phys. 14, 658-669 (2018).

8. A. P. Corfield, Mucins: A biologically relevant glycan barrier in mucosal protection. Biochim. Biophys. Acta. 1850, 236-252 (2015).

9. L. Z. Mi et al., Simultaneous visualization of the extracellular and cytoplasmic domains of the epidermal growth factor receptor. Nat. Struct. Mol. Biol. 18, 984-989 (2011).

10. D. Y. W. Lin et al., The PD-1/PD-L1 complex resembles the antigen-binding Fv domains

of antibodies and T cell receptors. Proc. Natl. Acad. Sci. USA 105, 3011-3016 (2008).

11. G. Fenalti et al., Structure of the human marker of self 5-transmembrane receptor CD47. Nat. Commun. 12, 5218 (2021).
12. C. V. Rao et al., Small-molecule inhibition of GCNT3 disrupts mucin biosynthesis and malignant cellular behaviors in pancreatic cancer. Cancer Res. 76, 1965-1974 (2016).
13. K. Pedram et al., Design of a mucin-selective protease for targeted degradation of cancer-associated mucins. Nat. Biotechnol. 42, 597-607 (2024).
14. S. A. Malaker et al., The mucin-selective protease StcE enables molecular and functional analysis of human cancer-associated mucins. Proc. Natl. Acad. Sci. USA 116, 7278-7287 (2019).
15. N. Villalba, S. Baby, S. Y. Yuan, The endothelial glycocalyx as a double-edged sword in microvascular homeostasis and pathogenesis. Front. Cell. Dev. Biol. 9, 711003 (2021).
16. R. L. Szabady, M. A. Lokuta, K. B. Walters, A. Huttenlocher, R. A. Welch, Modulation of neutrophil function by a secreted mucinase of Escherichia coli O157:H7. PLoS Pathog. 5, e1000320 (2009).
17. I. Levental, E. Lyman, Regulation of membrane protein structure and function by their

lipid nano-environment. Nat. Rev. Mol. Cell Biol. 24, 107-122 (2023).

18. X. Y. Lin, L. D. Yue, K. Cheng, L. Rao, Engineering cellular vesicles for immunotherapy. Acc. Mater. Res. 6, 327-339 (2025).
19. C. C. Zhao et al., Vesicular antibodies: Shedding light on antibody therapeutics with cell membrane nanotechnology. Adv. Mater. 35, e2207875 (2023).
20. G. Walsh, Biopharmaceutical benchmarks 2018. Nat. Biotechnol. 36, 1136-1145 (2018).
21. K. Lang, J. W. Chin, Cellular incorporation of unnatural amino acids and bioorthogonal labeling of proteins. Chem. Rev. 114, 4764-4806 (2014).
22. J. C. Wu, H. L. Lu, X. M. Xu, L. Rao, Y. Ge, Engineered cellular vesicles displaying glycosylated nanobodies for cancer immunotherapy. Angew. Chem. Int. Ed. 63, e202404889 (2024).
23. B. Zakeri et al., Peptide tag forming a rapid covalent bond to a protein, through engineering a bacterial adhesin. Proc. Natl. Acad. Sci. USA 109, 690-697 (2012).
24. G. Kim et al., Engineering modular enzyme assembly: synthetic interface strategies for natural products biosynthesis applications. Nat. Prod. Rep. 42, 1489-1506 (2025).
25. D. P. Arnold, Y. X. Xu, S. C. Takatori, Antibody binding reports spatial heterogeneities in

cell membrane organization. Nat. Commun. 14, 2884 (2023).

26. M. A. Goyette et al., Cancer-stromal cell interactions in breast cancer brain metastases induce glycocalyx-mediated resistance to HER2 targeting therapies. Proc. Natl. Acad. Sci USA 121, e2322688121 (2024).
27. Y. Zhou et al., T cell-derived apoptotic extracellular vesicles hydrolyze cGAMP to alleviate radiation enteritis via surface enzyme ENPP1. Adv. Sci. 11, e202401634 (2024).
28. C. Kofoed et al., Programmable protein ligation on cell surfaces. Nature 645, 793-800 (2025).
29. S. B. Willingham et al., The CD47-signal regulatory protein alpha interaction is a therapeutic target for human solid tumors. Proc. Natl. Acad. Sci. USA 109, 6662-6667 (2012).
30. H. Xiao, E. C. Woods, P. Vukojicic, C. R. Bertozzi, Precision glycocalyx editing as a strategy for cancer immunotherapy. Proc. Natl. Acad. Sci. USA 113, 10304-10309 (2016).
31. E. Rodríguez, S. T. T. Schetters, Y. van Kooyk, The tumour glyco-code as a novel

immune checkpoint for immunotherapy. Nat. Rev. Immunol. 18, 204-211 (2018).

32. A. D. Posey et al., Engineered CAR T cells targeting the cancer-associated Tn-glycoform of the membrane mucin MUC1 control adenocarcinoma. Immunity 44, 1444-1454 (2016).

33. J. M. Tarbell, L. M. Cancel, The glycocalyx and its significance in human medicine. J. Intern. Med. 280, 97-113 (2016).

34. B. A. H. Smith, C. R. Bertozzi, The clinical impact of glycobiology: targeting selectins, Siglecs and mammalian glycans. Nat. Rev. Drug Discov. 20, 217-243 (2021).

35. J. L. Lai et al., Triple hybrid cellular nanovesicles promote cardiac repair after ischemic reperfusion. ACS Nano 18, 4443-4455 (2024).

36. X. Xiong et al., Neoantigen-based cancer vaccination using chimeric RNA-loaded dendritic cell-derived extracellular vesicles. J. Extracell. Vesicles 11, e12243 (2022).

37. H. Yang et al., Molecular superglue-mediated higher-order assembly of TRAIL variants with superior apoptosis induction and antitumor activity. Biomaterials 295, 121994 (2023).

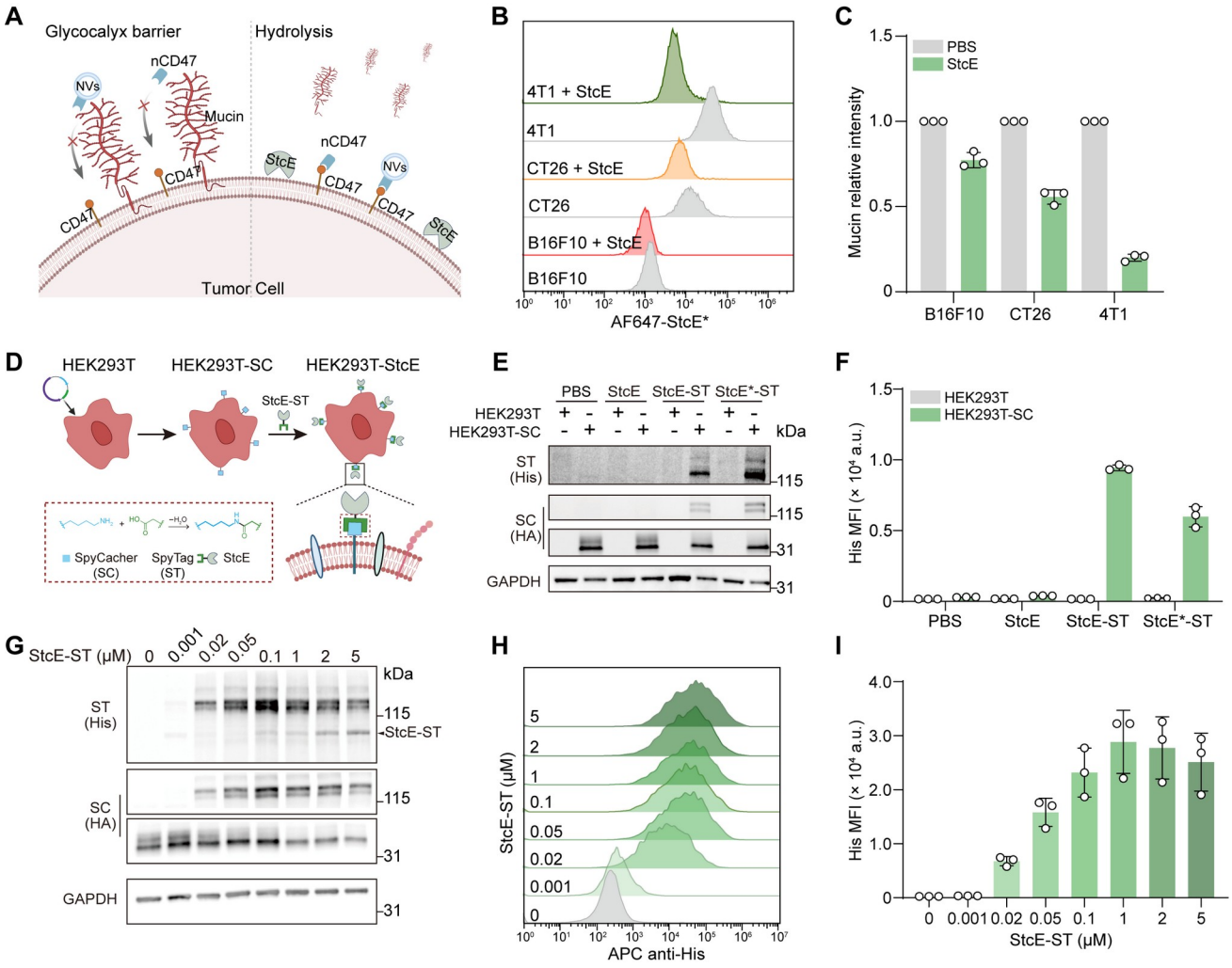

Fig. 1. Bioconjugation display of mucinase StcE on HEK293T cell surfaces. (*A*) Schematic illustration of mucinase-mediated degradation of the glycocalyx barrier, exposing the CD47 immune checkpoint to enhance binding of anti-CD47 nanobody (nCD47) or nCD47-conjugated NVs. (*B*) Flow cytometry analysis and (*C*) mean fluorescence intensity (MFI) quantification of mucin residues in the indicated cells treated with StcE, detected by Alexa Fluor 647 (AF647)-StcE* staining. (*D*) Schematic illustration of the bioconjugation reaction via SpyTag (ST)-SpyCatcher (SC) on SC-expressing HEK293T cells. (*E*) Western blot analysis of His- and HA-tagged proteins after incubation of StcE, StcE-ST, or StcE*-ST with HEK293T or HEK293T-SC cells. (*F*) MFI quantification of His-tagged proteins on cell surfaces after incubation with StcE, StcE-ST, or StcE*-ST, analyzed by live-cell flow cytometry using APC anti-His staining. (*G*) Western blot analysis of His-tagged StcE-ST on HEK293T-SC cells after incubation with increasing concentrations of StcE-ST (0-5 μM). (*H*) Flow cytometry analysis and (*I*) MFI quantification of His-tagged StcE-ST on SC-expressing cells after incubation with increasing concentrations of StcE-ST (0-5 μM). StcE*: inactive

point mutant. Data are presented as mean ± S.D. ($n = 3$)

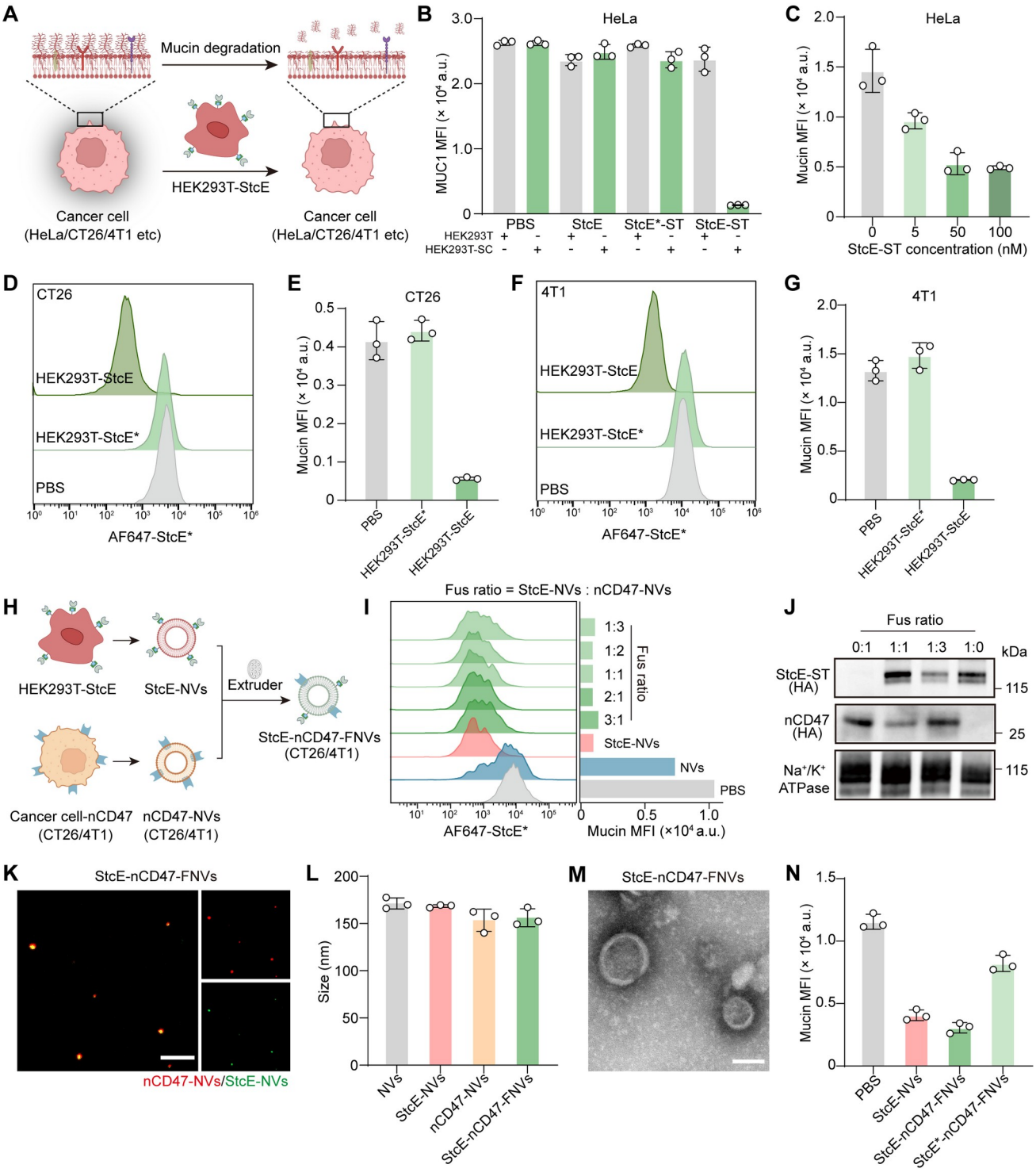

Fig. 2. Preparation and characterization of multifunctional NVs. (*A*) Schematic illustration of mucin degradation on cancer cell surfaces by HEK293T-StcE cells. (*B*) Mean fluorescence intensity (MFI) quantification of MUC1 on HeLa cells after incubation with HEK293T-StcE cells for 1 h, analyzed by live-cell flow cytometry using PE anti-MUC1 staining. (*C*) MFI quantification of mucin on HeLa cells after incubation with HEK293T-SpyCatcher (SC) cells conjugated with StcE-SpyTag (ST) at the indicated concentrations (5-100 nM) for 1 h, analyzed by live-

cell flow cytometry with Alexa Fluor 647 (AF647)-StcE* staining. (*D*) Flow cytometry analysis and (*E*) MFI quantification of mucin on CT26 cells after incubation with HEK293T-StcE cells, detected by AF647-StcE* staining. (*F*) Flow cytometry analysis and (*G*) MFI quantification of mucin on 4T1 cells after incubation with HEK293T-StcE cells, detected by AF647-StcE* staining. (*H*) Schematic illustration of the preparation of genetically programmable StcE-nCD47-FNVs. (*I*) MFI quantification of MUC1 on HeLa cells after incubation with StcE-nCD47-FNVs at different fusion ratios, analyzed by live-cell flow cytometry with PE anti-MUC1 staining. NVs are derived from HEK293T cells. (*J*) Western blot analysis of nCD47 and StcE-ST in nCD47-NVs, StcE-nCD47-FNVs (fusion ratio = StcE-NVs: nCD47-NVs), and StcE-NVs. (*K*) Confocal laser scanning microscopy (CLSM) images showing fusion of DiI-labeled nCD47-NVs (red) with DiO-labeled StcE-NVs (green). The appearance of a yellow signal indicates co-localization and successful fusion to form StcE-nCD47-FNVs. Scale bar, 5 μm. (*L*) Size distribution of NVs (derived from CT26 cells), StcE-NVs, nCD47-NVs, and StcE-nCD47-FNVs. (*M*) Transmission electron microscopy (TEM) image of StcE-nCD47-FNVs. Scale bar, 50 nm. (*N*) MFI quantification of mucin on CT26 cells after incubation with StcE-nCD47-FNVs at a 1:3 fusion ratio, analyzed by live-cell flow cytometry with AF647-StcE* staining. StcE*: inactive point mutant. Data are presented as mean ± S.D. ($n = 3$). All nCD47-NVs are from CT26-nCD47 cells.

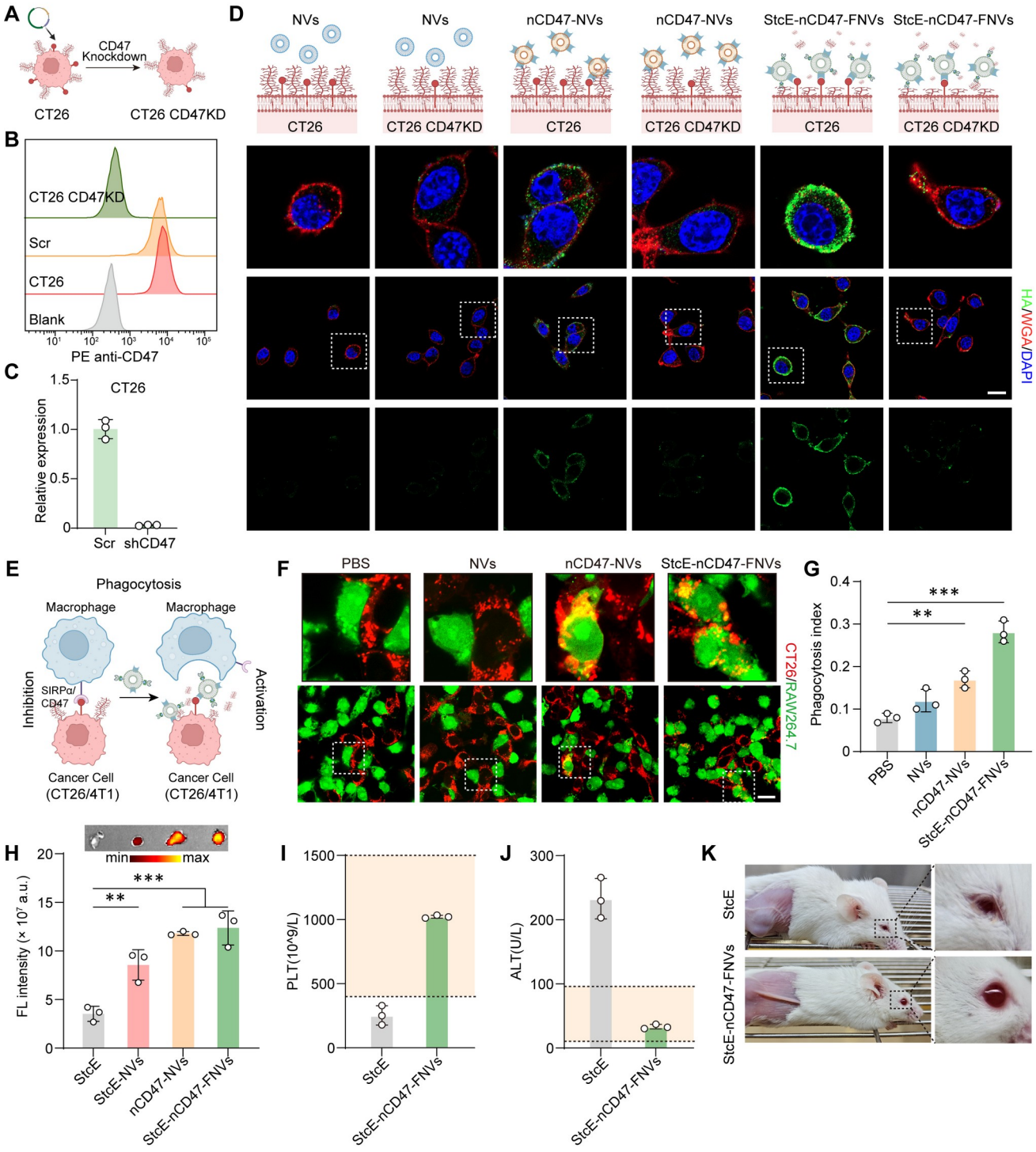

Fig. 3. StcE-nCD47-FNVs for targeted CD47 checkpoint blockade and biocompatibility assessment. (*A*) Schematic illustration of shRNA-mediated knockdown of CD47 expression in CT26 cells. (*B*) Flow cytometry analysis of CD47 protein levels in CT26 cells stably transfected with shScramble (shScr) or shCD47 RNA. (*C*) qPCR quantification of CD47 mRNA levels in CT26 cells stably transfected with shScr or shCD47 RNA. (*D*) Confocal imaging of nCD47-NVs or StcE-nCD47-FNVs binding to CD47 on CT26 cell surfaces. Scale bar, 20 μm. (*E*)

Schematic illustration showing how StcE-nCD47-FNVs overcome the CD47-SIRPα immune checkpoint to promote phagocytosis. StcE-nCD47-FNVs first degrade the tumor glycocalyx, enabling access to and blockade of the CD47, thereby triggering macrophage-mediated phagocytosis of cancer cells. (*F*) Fluorescence images of phagocytosis assays induced by the indicated NVs. RAW264.7 macrophages were stained with CFSE (green), and CT26 cells with eFluor670 (red). Scale bar, 20 μm. (*G*) Quantification of the phagocytosis index of CT26 cells by RAW264.7 macrophages. The phagocytosis index was calculated as the number of $CFSE^+$ tumor cells engulfed per 50 macrophages. (*H*) *In vivo* imaging and quantification of CT26 tumors from subcutaneous xenografts 48 h after intravenous injection of Cy5.5-labeled StcE, StcE-NVs, nCD47-NVs, or StcE-nCD47-FNVs at equivalent protein concentrations. (*I-J*) Hematological and serum biochemical analyses of treated mice. Shown are platelet (PLT) counts and alanine aminotransferase (ALT) levels, with normal ranges indicated by orange shading. (*K*) Representative photographs of ocular inflammation in mice following the different treatments. Data are presented as mean ± S.D. ($n = 3$) *P < 0.05, **$P < 0.01$, ***$P < 0.001$. NVs and nCD47-NVs are from CT26 and CT26-nCD47 cells.

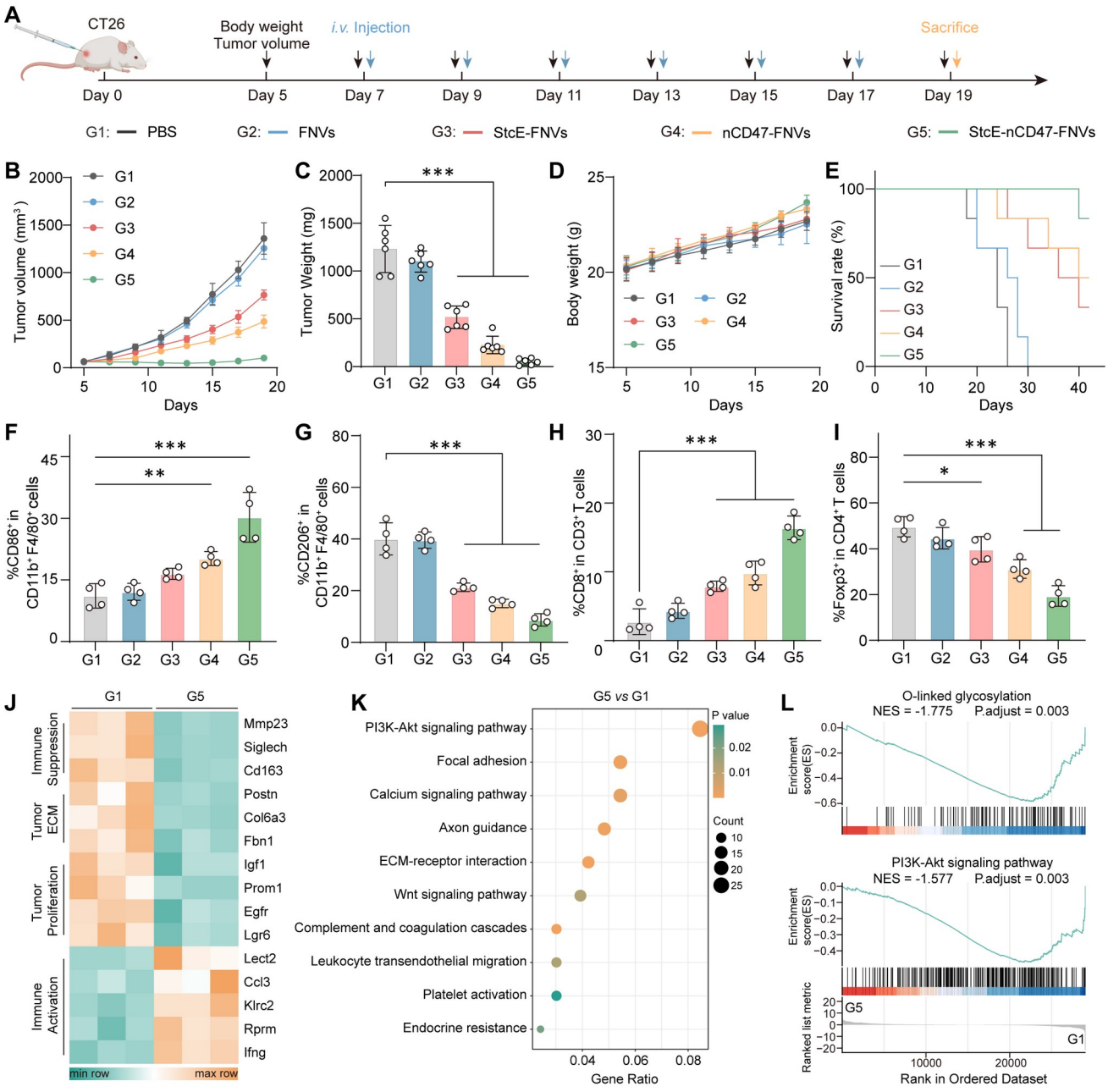

Fig. 4. *In vivo* antitumor efficacy of different treatments in CT26 tumor-bearing mice. (*A*) Schematic illustration of the experimental design and treatment schedule. CT26 tumor-bearing mice received six intravenous injections (blue arrows) of the indicated formulations beginning on day 7. Tumor volume and body weight were monitored (black arrows) until sacrifice on day 19. The five groups were: G1 (Blank), G2 (FNVs), G3 (StcE-FNVs), G4 (nCD47-FNVs), and G5 (StcE-nCD47-FNVs). (*B*) Tumor growth curves, (*C*) tumor weights at study endpoint, (*D*) body weight changes, and (*E*) survival curves. (*F-I*) Quantitative analysis of tumor-infiltrating immune cells, including (*F*) $CD11b^+CD86^+$ macrophages, (*G*) $CD11b^+CD206^+$ macrophages, (*H*) $CD3^+CD8^+$ T cells, and (*I*) $CD4^+Foxp3^+$ T cells. (*J*) Heatmap of differentially expressed genes

(DEGs, FDR-corrected $P < 0.05$) associated with immune suppression, immune activation, tumor proliferation, and extracellular matrix (ECM) in CT26 tumors from Blank and StcE-nCD47-FNVs-treated mice. (*K*) KEGG pathway enrichment analysis of DEGs between StcE-nCD47-FNVs-treated and Blank groups. (*L*) Gene Set Enrichment Analysis (GSEA) plots in StcE-nCD47-FNVs-treated tumors compared with Blank controls. Data are presented as mean ± S.D. (*B-E, n* = 6; *F-I, n* = 4; *J-L, n* = 3). $^{*}P < 0.05$, $^{**}P < 0.01$, $^{***}P < 0.001$. FNVs (HEK293T-NVs: CT26-NVs =1:3, no functional proteins), StcE-FNVs (HEK293T-StcE-NVs: CT26-NVs =1:3, glycocalyx hydrolysis only), nCD47-FNVs (HEK293T-NVs: CT26-nCD47-NVs =1:3, CD47 blockade only), StcE-nCD47-FNVs (HEK293T-StcE-NVs: CT26-nCD47-NVs =1:3, combination).

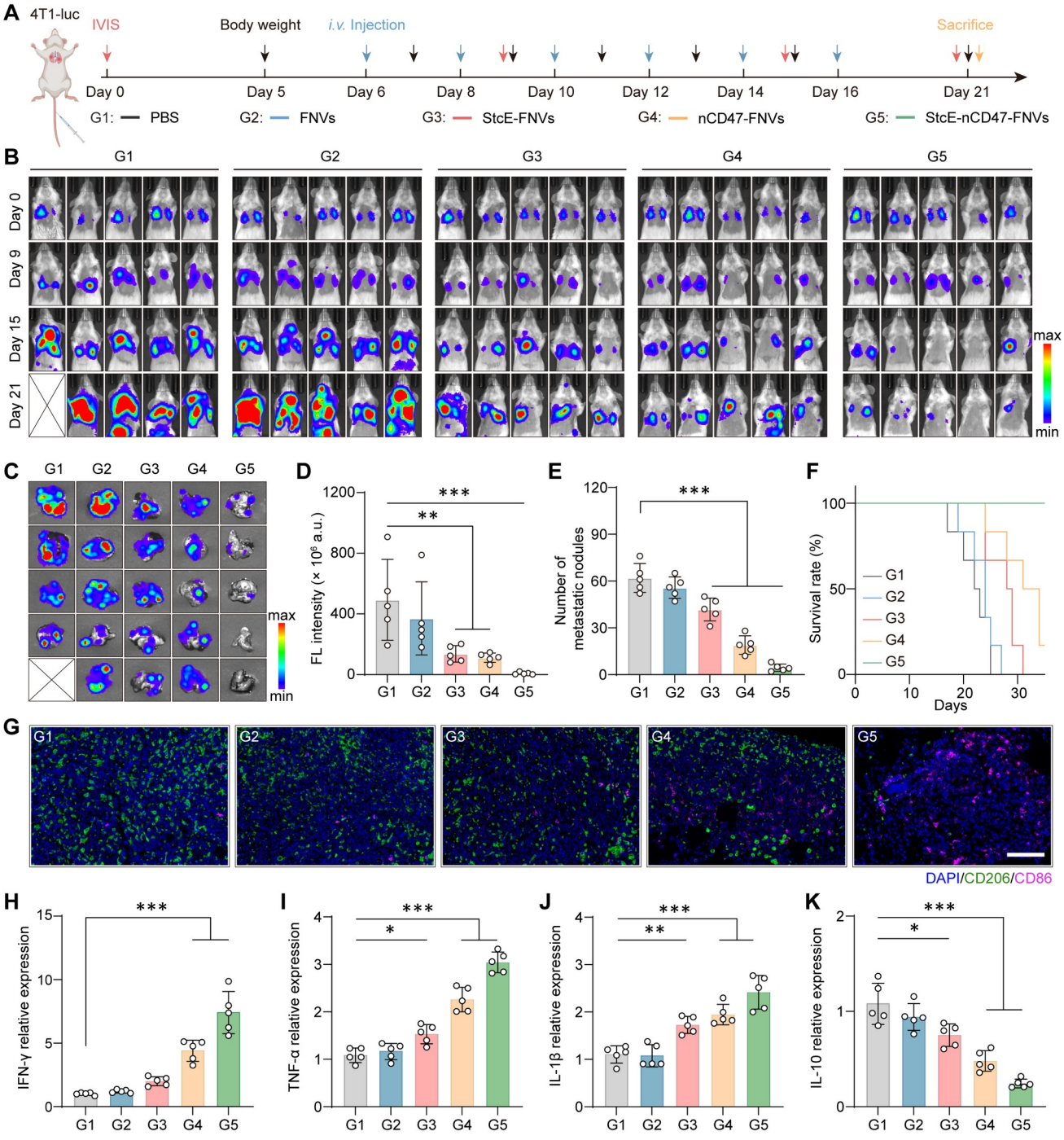

Fig. 5. *In vivo* antitumor efficacy in a 4T1 lung metastasis model. (*A*) Schematic illustration of the experimental design. The 4T1 lung metastasis model was established by intravenous injection of 4T1-luc cells. From day 6, mice received six doses of the indicated formulations every other day (blue arrows). Tumor burden was monitored by *in vivo* imaging system (IVIS, red arrows), and body weight was measured throughout (black arrows). The five groups were: G1 (Blank), G2 (FNVs), G3 (StcE-FNVs), G4 (nCD47-FNVs), and G5 (StcE-nCD47-FNVs). (*B*) Representative IVIS bioluminescence images of tumor-

bearing mice on days 0, 9, 15, and 21, showing tumor progression. (*C*) *Ex vivo* bioluminescence imaging of excised lungs at endpoint. (*D*) Quantification of lung bioluminescence intensity and (*E*) number of metastatic nodules. (*F*) Kaplan-Meier survival curves of mice receiving different treatments. (*G*) Immunostaining of macrophage infiltration in lung tumors across treatment groups. Scale bar, 100 μm. (*H-K*) RT-qPCR analysis of intratumoral cytokine mRNA expression levels, including pro-inflammatory cytokines (*H*) IFN-γ, (*I*) TNF-α, (*J*) IL-1β, and the anti-inflammatory cytokine (*K*) IL-10. Data are presented as mean ±S.D. ($n = 5$) $^{*}P < 0.05$, $^{**}P < 0.01$, $^{***}P < 0.001$. FNVs (HEK293T-NVs: 4T1-NVs =1:3, no functional proteins), StcE-FNVs (HEK293T-StcE-NVs: 4T1-NVs =1:3, glycocalyx hydrolysis only), nCD47-FNVs (HEK293T-NVs: 4T1-nCD47-NVs =1:3, CD47 blockade only), StcE-nCD47-FNVs (HEK293T-StcE-NVs: 4T1-nCD47-NVs =1:3, combination).